Design of Cold-formed High Strength Steel Diamond Bird-beak Tubular T- and X-Joints

Madhup Pandey[1]; and Ben Young[2], F.ASCE

Abstract

Numerical investigation and design of cold-formed high strength steel (CFHSS) diamond bird-beak (DBB) T- and X-joints are presented in this paper. The 0.2% proof stress of braces and chords was 960 MPa. Tests of CFHSS DBB T- and X-joints undergoing compression loads were carried out by Pandey and Young (2021a and 2022). The test results were used to develop accurate finite element (FE) models in this study. A comprehensive FE parametric study was then performed using the verified FE models. The nominal strengths predicted from the literature and European code were compared to the joint failure strengths and ultimate capacities of 244 DBB T- and X-joints specimens, including 224 FE specimens investigated in this work. The failure of DBB T- and X-joints specimens at chord crown locations was identified as the dominant failure mode. It has been shown that the design provisions given in the literature and European code are unsuitable and uneconomical for cold-formed S960 steel grade DBB T- and X-joints investigated in this study. Hence, accurate, less dispersed and reliable design equations are proposed in this work, using two design approaches, to predict the joint failure strengths and ultimate capacities of the investigated DBB T- and X-joints.

Keywords: *Cold-formed steel; Design rules; Diamond bird-beak joints; FE analysis; High strength steel; S960 steel, Tubular joints.*

[1] Assistant Professor, Department of Civil Engineering, University of Nottingham, Nottingham, United Kingdom. (Corresponding author) E-mail: madhup.pandey@nottingham.ac.uk
[2] Professor, Department of Civil and Environmental Engineering, The Hong Kong Polytechnic University, Hong Kong, China. E-mail: ben.young@polyu.edu.hk

Introduction

Bird-beak joints are one of the novel configurations of hollow section joints. The diamond bird-beak (DBB) configuration is obtained by rotating the brace and chord members about their respective centroidal axes. In addition to the aesthetic superiority of this configuration, it also brings many other technical advantages, including (a) smooth transfer of load from brace to chord members, which averted the development of bending and buckling in chord member; (b) high stiffness around the brace-chord junction; (c) less hindrance for wind loads; and (d) enhanced ultimate capacities of joints. The practical applications of DBB joints can be seen in the convention centre in Minneapolis (Minnesota, USA), national stadium (Beijing, China) and Takishita bridge (Ibaraki, Japan).

High strength steel (HSS) (in this study, referred to steels with steel grades higher than S460) circular, square and rectangular hollow sections (CHS, SHS and RHS) members are in high demand in various civil engineering projects because of their superior strength per unit weight, reduced handling cost and reduced erection time. However, the lack of adequate research work and design recommendations are the primary reasons hampering the widespread use of HSS tubular members. Nonetheless, some studies have recently been conducted to investigate the structural performance of HSS open section members (Wang et al. 2019 and 2020), tubular members (Li and Young, 2018 and 2019; Ma et al., 2016, 2017, 2019 and 2021), built-up box section joints (Lan et al. 2019 and 2020), and cold-formed high strength steel (CFHSS) tubular joints (Pandey and Young, 2020, 2021b, 2021c, 2021d and 2021e).

The DBB joint configuration was first introduced by Ono et al. (1991), where DBB K- and T-joints made of SHS (hereafter, RHS also represents SHS) were tested to determine their static strengths. Using test results, semi-empirical design equations were proposed to predict the static ultimate capacities of normal strength steel (in this study, referred to steels with steel grades lower than or equal to S460) DBB K- and T-joints. Numerical and analytical methods were used by Davies et al. (1996) and Davies and Kelly (1995) to determine the ultimate capacities of S275 steel grade DBB K-, X- and T-joints. In addition, Kelly (1998) used the numerical method to study the influence of member rotation on the static strengths of S275 steel grade K-, X-, and T-joints. A comparative numerical investigation between conventional (RHS and CHS joints) and DBB X-joints made of S275 steel grade was carried out by Owen et al. (2001). The numerical results obtained after assuming an elasto-plastic material behaviour were used to propose a design equation to predict the static ultimate capacities of S275 steel grade DBB X-joints. The numerical work conducted by Owen et al. (2001) was extended by Peña and Chacón (2014) by investigating the effects of different steel grades (S235, S275 and S460) on the ultimate capacities of DBB X-joints. Subsequently, an improved design equation was proposed for the static ultimate capacities of DBB X-joints with steel grades up to S460. Chen and Wang (2015) performed a detailed numerical parametric study on Q235 steel grade DBB T-joints and proposed a design equation for the static ultimate capacities of the investigated joints.

This literature review confirmed that no research is available on CFHSS DBB T- and X-joints, except for the experimental investigations carried out by Pandey and Young (2021a and 2022). The test results were used to develop accurate finite element (FE) models of DBB T- and X-joints in this study. Subsequently, a comprehensive FE parametric study, comprising 224 FE analyses, was performed using the verified FE models. The nominal strengths predicted using the equations in the literature (Chen and Wang, 2015; Ono et al., 1991; Peña and Chacón, 2014) and EC3 (2021) were evaluated with respect to the joint failure strengths (N_f) and ultimate capacities (N_{max}) of DBB T- and X-joints test and FE specimens. The existing design rules have been demonstrated to be unsuitable for the range of DBB joints investigated in this work. Hence, using two design approaches, new, economical and reliable design rules are proposed in this work to estimate the N_f and N_{max} of cold-formed S960 steel grade DBB T- and X-joints.

Summary of experimental investigations

The static behaviour of cold-formed S960 steel DBB T- and X-joints were experimentally studied by Pandey and Young (2021a and 2022). Axial compression loads were applied on the DBB T- and X-joints test specimens via braces. The chord ends of DBB T-joint test specimens were supported on rollers through specially fabricated V-shaped end blocks, while braces of DBB X-joint test specimens were fixed at both ends. The braces and chords were made of S960 steel grade RHS members. A fully robotic metal active gas welding was employed to weld braces and chords. In total, 20 tests were conducted, including 10 DBB T-joints and 10 DBB X-joints. Moreover, chord ends were not welded to end plates and were freely deformed during the tests. Figs. 1(a) and 1(b) present various notations for DBB T- and X-joints, respectively. The static strengths of DBB T- and X-joints primarily depend on non-dimensional geometric ratios, including β' (b_1'/b_0'), 2γ (b_0/t_0) and τ (t_1/t_0). The symbols b, h, t and R stand for cross-section width, depth, thickness and external corner radius of RHS member, respectively. The subscripts 0 and 1 denote chord and brace, respectively. In the test programs, β' varied from 0.40 to 0.65, 2γ varied from 25.5 to 39.0 and τ varied from 0.67 to 1.28. The lengths of braces (L_1) of DBB T- and X-joints were determined as $2\sqrt{b_1^2+h_1^2}$ mm. On the other hand, the lengths of chords (L_0) of DBB T- and X-joints were determined as $h_1'+3h_0'+180$ mm and $h_1'+4h_0'$ mm, respectively. The symbols b_1' and h_1' stand for effective width and depth of brace cross-section, respectively. On the other hand, the symbols b_0' and h_0' stand for effective width and depth of chord cross-section, respectively. For SHS brace, b_1' and h_1' were equal to $\sqrt{b_1^2+h_1^2}$ – $0.83R_1$. However, for RHS brace, b_1' and h_1' are equal to $2\max[b_1,h_1]\sin\omega - 0.83R_1$ and $\sqrt{b_1^2+h_1^2}$ – $0.83R_1$, respectively. For chord member, b_0' and h_0' were equal to $\sqrt{b_0^2+h_0^2}$ – $0.83R_0$. The measured static 0.2% proof stresses of RHS members varied between 952 to 1059 MPa, while the measured static 0.2% proof stress of welding filler material was 965 MPa. The chord crown failure (C) mode was identified as the dominant failure mode for all test specimens. Moreover, the N_f of all test specimens was governed by the ultimate deformation limit (i.e. 0.03 b_0') criterion. The test results were obtained in the form of N vs u curves, where N and u respectively stand for static load and chord indentation at the crown location. The typical member-rotation angles (ω) along the centroidal axis of the brace member are shown in Fig. 1(c).

Numerical investigation

Finite element models

General

One of the popular FE software, ABAQUS (2017), was used to perform comprehensive FE analyses in this study. As the induced strains in the FE model during the applied load were unidirectional (i.e. no load reversal), the isotropic strain hardening law was selected for the analysis. The yielding onsets of FE models in this study were based on the von-Mises yield theory. In the FE analyses, the growth of the time step was kept non-linear to reduce the overall computation time. Furthermore, the default Newton-Raphson method was used to find the roots of non-linear equilibrium equations. In addition to the accuracy associated with the Newton-Raphson method, one of the popular benefits of using this numerical technique is its quadratic convergent approach, which in turn significantly increases the convergence rate of non-linear problems. The material non-linearity was considered in the FE models by assigning the measured values of static stress-strain curves of flat and corner regions of RHS members in the plastic material definition part of the FE model. On the other hand, the geometric non-linearities in FE models were considered by enabling the non-linear geometry parameter (*NLGEOM) in ABAQUS (2017), which in turn allow FE models to undergo large displacement during the analyses. Furthermore, various factors, including through-thickness division, contact interactions, mesh seed spacing, corner region extension and element types, were also studied and discussed in the following sub-sections of this paper. The labelling of parametric DBB T- and X-joint FE specimens was kept identical to the label system used in the test programs (Pandey and Young, 2021a and 2022).

Material properties, element type and mesh size

The test specimens of the experimental programs (Pandey and Young, 2021a and 2022) were fabricated from tubular members that belonged to the same batch of tubes used in other investigations conducted by Pandey and Young (2019a, 2019b, 2020, 2021b, 2021c, 2021d and 2021e). Additionally, Pandey and Young (2019b) investigated the material properties of welding filler material. The details pertaining to the material properties of welding filler material and tubular members can be referred to Pandey and Young (2019a and 2019b). The inclusions of static stress-strain curves in FE models helped avert the effect of loading rate from FE results. The true stress-strain curves of welding filler material as well as flat and corner portions of RHS members were allocated to the corresponding parts of the FE specimens. In this study, the influence of cold-working in RHS members was included in FE models by assigning wider corner regions. Various distances for corner extension in RHS members were considered in the sensitivity analyses, and finally, the corner portions were elongated by $2t$ into the neighbouring flat portions, which was in agreement with other studies conducted on CFHSS tubular members and joints (Pandey et al. 2021a and 2021b; Liu et al. 2021; Xu et al. 2017). Except for the welds, all other parts of the FE models were developed using the C3D20 element. On the other hand, the C3D10 element was used to model the weld parts due to their complicated shapes. The use of solid elements helped in making realistic fusions between tubular and weld parts of DBB T- and X-joints FE models.

Convergence studies were conducted using different mesh sizes, and finally, chord and brace members were seeded at 4 mm and 7 mm intervals, respectively, along both longitudinal and transverse directions. Moreover, the seeding intervals of weld parts reciprocated the seeding spacings of their respective brace parts. In order to ensure the smooth transfer of stresses between the flat portions of the RHS cross-section, the corner portions of the RHS cross-section were split into ten elements. FE analyses were also conducted to examine the influence of divisions along the wall thickness (t) of RHS members. The results of these FE analyses demonstrated the trivial influence of wall thickness divisions on the load vs chord indentation curves of the investigated DBB T- and X-joints. The use of the C3D20 element having one built-in node along the thickness direction as well as the small wall thickness of test specimens (i.e. $t \leq 6$ mm) led to such observations. The presence of a built-in node naturally provides one division along the wall thickness of tubular members (i.e. two layers). It is worth noting that a similar observation was also noticed in other studies (Crockett, 1994; Pandey et al., 2021a and 2021b). Thus, for the validations of DBB T- and X-joints FE models, the wall thicknesses of tubular members were kept undivided.

Modelling of welds and contact interactions

The dihedral angle between brace and chord members of a DBB joint is 120°, as shown in Fig. 2. According to the weld design recommendations given in EC3 (2005), CIDECT (2009) and AWS D1.1M (2020), the fillet weld can be used up to the maximum dihedral angle equal to 120°, therefore, fillet weld was modelled for all FE specimens investigated in this study. The welds were modelled using the average values of measured fillet weld leg sizes. The inclusions of weld geometries and weld material properties appreciably improved the overall accuracies of DBB T- and X-joints FE models. Furthermore, weld component modelling aided in achieving realistic load transfer between brace and chord members. The selection of the C3D10 element maintained optimum stiffness around the joint perimeter due to its ability of taking complicated shapes. A total of two types of contact interactions was defined in DBB T- and X-joints FE models. First, contact interaction between brace and chord members of DBB T- and X-joints FE models. Second, contact interaction between chord members and V-shaped end blocks of DBB T-joint FE models. In addition, a tie constraint was also established between weld and tubular members of DBB T- and X-joints FE models. Both contact interactions were established using the built-in surface-to-surface contact definition. The contact interaction(s) between brace and chord members of DBB T- and X-joints FE models was kept frictionless, while a frictional penalty of 0.3 was imposed on the contact interaction between chord member and V-shaped end blocks of DBB T-joint FE models. Along the normal direction of these two contact interactions, a 'hard' contact pressure overclosure was used. In addition, finite sliding was permitted between the interaction surfaces. This technique of fusion between various parts of FE models has been successfully used in several other investigations (Pandey et al., 2021a and 2021b; Hu et al., 2021; Li and Young, 2022a and 2022b).

Boundary conditions

The boundary conditions in DBB T- and X-joints FE models were assigned by creating reference points. Three reference points were created for the DBB T-joint FE model, including one top reference point (TRP) and two bottom reference points (BRP-1 and BRP-2). The TRP replicated the fixed boundary condition of the top brace end, while BRP-1 and BRP-2 replicated the boundary conditions of the roller positioned at each chord end. As shown in Fig. 3, the TRP was created at the cross-section centre of the top brace end and BRP-1 and BRP-2 were created at 20 mm below the centre of the bottom surfaces of V-shaped end blocks. The TRP, BRP-1 and BRP-2 were then coupled to their corresponding surfaces using a built-in kinematic coupling type.

In order to exactly replicate the boundary conditions of the DBB T-joint test setup, all degrees of freedom (DOF) of TRP were restrained. On the other hand, for BRP-1 and BRP-2, except for the translations along the vertical and longitudinal directions of the DBB T-joint FE specimen as well as the rotation about the chord width direction, all other DOF of BRP-1 and BRP-2 were also restrained. In addition, all DOF of other nodes of DBB T-joint FE specimens were kept unrestrained for both rotation and translation. On the other hand, in DBB X-joint FE model, the top and bottom reference points (TRP and BRP) were created at the cross-section centres of braces, as shown in Fig. 4. Subsequently, TRP and BRP were coupled to their respective brace end cross-section surfaces using kinematic coupling type. In order to exactly replicate the boundary conditions of the DBB X-joint test setup, all DOF of TRP were restrained. However, except for the translation along the vertical direction of the DBB X-joint specimen, all other DOF of BRP were also restrained. Moreover, all DOF of other nodes of the DBB X-joint FE specimen were kept unrestrained for both rotation and translation. Using the displacement control method, compression load was then applied at the bottom reference points of the DBB T- and X-joints FE models. Following this approach, the boundary conditions and load application in FE analyses were identical to the test programs (Pandey and Young 2021a and 2022).

Weld heat affected region (WHAR)

The heat transferred to parent tubular members during the welding process has a considerable impact on the overall behaviour of hollow section joints (Pandey et al. 2021a). The design rules in international standards (AISC 360, 2016; ISO 14346, 2013; IIW, 2012; CIDECT, 2009; EC3, 2005) are identical for HSS produced from different methods, namely by adding alloying elements and by various heat treatment techniques. However, it has been reported in some recent studies (Pandey and Young, 2021c; Stroetmann et al., 2018; Javidan et al., 2016; Amraei et al., 2019 and 2020) that HSS produced by different methods exhibited different extents of softening around the welds. Investigations carried out by Stroetmann et al. (2018), Javidan et al. (2016) and Amraei et al. (2019 and 2020) reported 16% to 32% reductions in the ultimate strengths of S960 steel grade parent materials around the welds.

Pandey and Young (2021c) examined the material properties of the weld heat affected region (WHAR) of RHS members with 0.2% proof stress of 960 MPa and wall thickness varying between 3-6 mm. A 14% to 32% reduction in the ultimate strengths of the parent metals was reported in the first 6 mm distance of the WHAR. The definition of WHAR for tubular joints was proposed by Pandey et al. (2021a), as shown in Fig. 5. For DBB T- and X-joints FE models, the spreads of WHAR are shown in Figs. 3 and 4, respectively. In addition, a simplified strength reduction (S_{rl}) model was proposed by Pandey et al. (2021a) for S900 and S960 steel grades tubular joints to integrate the material properties of WHAR in FE models, as illustrated in Fig. 6. The proposed strength reduction model was successfully used to perform the numerical investigation and design of CFHSS T- and TF-joints (Pandey et al. 2021a and 2021b). Therefore, it was also included in this investigation, and accordingly, material properties were assigned to the WHAR of DBB T- and X-joints FE models. The adoption of WHAR appreciably improved the accuracies of FE models and, thus, the numerical results.

Validations of DBB T- and X-joints FE models

The DBB T- and X-joints FE models were developed using the modelling approaches described in the preceding sections of this paper. The test results of DBB T- and X-joints reported in Pandey and Young (2021a and 2022) were used to validate their corresponding FE models. The validations were performed by comparing the N_f, N_{max}, load-chord indentation histories and failure modes of test and FE specimens. The measured dimensions of tubular members and welds were used to develop all DBB T- and X-joints FE models. In addition, measured material properties of tubular members, welds and WHAR were also included. The N_f and N_{max} of DBB T- and X-joints test specimens were compared to those predicted from their corresponding FE models ($N_{f,FE}$ and $N_{max,FE}$). Referring to Table 1, when the joint failure strengths of DBB T-joint ($N_{f,T}$) test specimens were compared to the strengths predicted from DBB T-joint FE models, the mean (P_m) and coefficients of variation (COV) (V_p) of the overall comparisons were 0.98 and 0.022, respectively. However, when the ultimate capacities of DBB T-joint ($N_{max,T}$) test specimens were compared to the FE strengths, the mean (P_m) and COV (V_p) of the overall comparisons were 1.01 and 0.007, respectively.

When the joint failure strengths of DBB X-joint ($N_{f,X}$) test specimens were compared to the strengths predicted from DBB X-joint FE models, the mean (P_m) and COV (V_p) of the overall comparisons were 1.01 and 0.020, respectively. However, when the ultimate capacities of DBB X-joint ($N_{max,X}$) test specimens were compared to the FE strengths, the mean (P_m) and COV (V_p) of the overall comparisons were 1.01 and 0.016, respectively. Likewise in the experimental investigation, the N_f of DBB T- and X-joints was determined by jointly considering the ultimate capacity and ultimate deformation limit (i.e. $0.03\, b_0^{'}$) loads, whichever occurred earlier in the load vs chord indentation curves. In addition, the comparisons of N vs u curves between typical DBB T- and X-joints test and FE specimens are shown in Figs. 7 and 8, respectively. Moreover, Figs. 9 and 10 present the comparisons of failure modes between typical DBB T- and X-joints test and FE specimens, respectively. Therefore, from Table 1 and Figs. 7-10, it can be concluded that the validated FE models precisely replicated the overall static behaviour of DBB T- and X-joints.

Parametric study

Introduction

The test results reported in Pandey and Young (2021a and 2022) were not sufficient to develop a broad understanding of various governing factors affecting the static strengths of CFHSS DBB T- and X-joints. Therefore, the data pool was widened by performing a comprehensive numerical parametric study using the validated DBB T- and X-joints FE models. In total, 224 parametric FE analyses were performed in this study, including 112 DBB T-joints and 112 DBB X-joints. Table 2 presents the overall ranges of various critical parameters considered in the numerical parametric study. It is important to mention that, in this study, the

$0.03b_0'$ deformation limit criterion governed the N_f of all DBB FE specimens. In the parametric study, four member-rotation angles (ω) were included for braces (ω = 15°, 25°, 40° and 45°), while for all chords, ω was equal to 45°. All FE modelling techniques used in the validations of DBB T- and X-joints were also employed in the parametric study.

FE modelling details

In the numerical investigation, the dimensions of tubular members included practical sizes. Overall, the values of cross-section width and depth of braces and chords of parametric FE specimens varied between 40 mm to 200 mm, while wall thickness of braces and chords varied between 2.5 mm to 12 mm. The exterior corner radii of RHS brace and chord members (R_1 and R_0) conformed to the commercially produced HSS members (SSAB, 2017a and 2017b). In this study, R_1 and R_0 were kept as $2t$ for $t \leq 6$ mm, $2.5t$ for $6 < t \leq 10$ mm and $3t$ for $t > 10$ mm, which in turn also meet the limits detailed in EN 10219-2 (2019). The brace and chord lengths of DBB FE specimens were identical to those adopted in the experimental programs (Pandey and Young, 2021a and 2022). For meshing along the longitudinal and transverse directions of RHS members, seedings were approximately spaced at the minimum of [b/30, h/30], where b and h stand for cross-section width and depth of RHS member. Overall, the adopted mesh sizes of parametric FE specimens varied between 3 mm to 10 mm. On the other hand, the seeding interval of weld parts of parametric FE specimens reciprocated the seeding interval of their corresponding brace parts. For RHS members with $t \leq 6$ mm, no divisions were made along the wall thickness of braces and chords. However, for RHS members with $t > 6$ mm, the wall thickness of braces and chords was divided using a node. The use of the C3D20 element and one division along the wall thickness of FE specimens with $6 < t \leq 12$ provided four layers along the thickness direction. Further wall thickness divisions made the element assembly quite complex and led to unconverged results.

Following the prequalified tubular joint details given in AWS D1.1M (2020), the leg size (w) of FW of DBB T- and X-joints FE specimens was designed as 1.5 times the minimum of t_1 and t_0. The weld designs of both DBB T- and X-joints FE specimens were consistent with the experimental programs (Pandey and Young, 2021a and 2022). In the parametric study, the material properties of flat and corner portions of RHS 150×150×6 were assigned to the flat and corner portions of braces and chords of FE specimens. Besides, weld parts of all DBB T- and X-joints parametric FE specimens were given the measured material properties of welding filler material. Table 3 presents the measured material properties of RHS 150×150×6 and welding filling material adopted in the parametric study, which include Young's modulus (E), 0.2% proof stress and strain ($\sigma_{0.2}$ and $\varepsilon_{0.2}$), ultimate stress and strain (σ_u and ε_u), fracture strain (ε_f) and Ramberg-Osgood parameter (n). On the other hand, the material properties and spread of WHAR were in accordance with the recommendations proposed by Pandey et al. (2021a). In this study, the ignorance of WHAR in FE analyses of DBB T-joints over-estimated the N_f and N_{max} in the range of 8.1% to 29.9% and 6.7% to 31.0%, respectively. On the other hand, for DBB X-joints, the ignorance of WHAR in FE analyses over-estimated the N_f and N_{max} in the range of 7.1% to 63.3% and 3.5% to 19.1%, respectively.

Influence of governing geometric parameters and failure mode

With the increase of β' ratio, the brace member(s) extends up to a greater depth on the chord connecting regions. As a result, the chord member of DBB T- and X-joints suffered more local plastic deformation, which in turn enhanced both N_f and N_{max}. On the other hand, initial stiffness, N_f and N_{max} of DBB T- and X-joints decreased as 2γ ratio increased. The increase of 2γ ratio reduced the out-of-plane bending stiffness of chord connecting flanges, which in turn reduced the load bearing capacity of DBB joints. With regard to the effect of τ ratio, the stiffness and strength of DBB T- and X-joints first increased with the increase of τ ratio up to τ=1.0 and then decreased. Generally, for small values of τ ratio ($\tau < 0.50$), the joint could fail by the local buckling of brace member(s). However, for large values of τ ratio ($\tau > 2.0$), punching failure at chord crown and saddle locations could take place. For the design of tubular joints, generally, brace and chord members of identical nominal thicknesses (i.e. $\tau = 1.0$) are selected. For DBB joints, the value of ω of chord member is fixed and equal to 45°. However, generally, the N_f and N_{max} increased with the increase of the value of ω of brace member.

All DBB T- and X-joints test (Pandey and Young, 2021a and 2022) and FE specimens were failed by chord crown failure mode, which was denoted by the letter 'C'. In the chord crown failure (C) mode, the test and FE specimens were failed by predominant convex deformation at the crown locations of the chords. It is important to note that this failure mode was defined corresponding to the N_f of DBB T- and X-joints, which in turn was computed by combinedly considering the ultimate capacity and deformation limit loads, whichever occurred earlier in the N vs u curve. It is noteworthy to mention that the convex deformation at the chord crown location of all DBB T- and X-joint test and FE specimens was always larger than the corresponding concave deformation at the chord saddle location. The predominance of deformation at crown location remained valid for both the N_f and N_{max} of DBB T- and X-joints test and FE specimens. The deformation capacities of the DBB T- and X-joints test and FE specimens were significantly large. The attainment of the N_{max} of test and FE specimens was accompanied by large deformation at the crown and saddle regions of the chords. Generally, the N vs u curves of the DBB test and FE specimens entered a stagnant phase near the N_{max}, followed by a very gradual load drop in the post-ultimate regions. It should be stressed that for all DBB T- and X-joints test and FE specimens, the $0.03\,b_0^{'}$ loads occurred quite earlier than their corresponding ultimate capacities. In this investigation, the test and parametric FE specimens were failed by the C mode for $0.20 \leq \beta' \leq 0.84$. Moreover, none of the test and FE specimens were failed by the global buckling of braces.

It should be noted that, in the experimental investigations (Pandey and Young, 2021a and 2022) and in this study, DBB T- and X-joints were purposely designed for failure in the chord member. However, DBB T- and X-joints undergoing axial load (compression or tensile) through brace members could also fail by other failure modes, including local buckling of braces, combination of local buckling of braces and chord failure, and weld rupture failure. The DBB T- and X-joints undergoing brace axial compression load could fail by local buckling of braces for small values of τ ratio ($\tau < 0.50$). In addition, DBB T- and X-joints with small values of τ ratio and large values of 2γ ratio could fail by the combination of local buckling of braces and chord failure. Moreover, DBB T- and X-joints with inadequate weld design and subjected to tensile loads could fail by the rupture of welds, i.e. weld rupture failure.

Existing design rules

Currently, DBB joint configuration is not included in any international code of practice. The overall static behaviour of tubular T- and X-joints when subjected to axial compression loads via braces are nearly similar. Therefore, in this investigation, the N_f and N_{max} of test and parametric FE specimens were evaluated against the nominal strengths of DBB T- and X-joints design rules given in the literature (Chen and Wang, 2015; Ono et al., 1991; Peña and Chacón, 2014). Moreover, owing to the rotated brace and chord members of DBB T- and X-joints, the DBB joint configuration resembles to that of the CHS-to-CHS configuration. Thus, the N_f and N_{max} of test and parametric FE specimens were also evaluated against the nominal strengths of CHS-to-CHS T- and X-joint design rules given in EC3 (2021). The nominal strengths were determined using the measured dimensions and mechanical properties. Under axial compression load, the chord members of DBB T-joints were subjected to chord-in-plane bending. In this investigation, the effect of normal stresses developed due to chord-in-plane bending on the static strengths of DBB T-joints was considered through chord stress functions (k_n, $f(n')$ and Q_f). On the other hand, in this study, no preload was applied to the chord members of DBB X-joints. Therefore, the values of k_n, $f(n')$ and Q_f for DBB X-joints were set to unity in Eqs. (1) to (5).

Ono et al. (1991)

Ono et al. (1991) experimentally studied the static behaviour of DBB T-joints with yield strengths varied between 365-415 MPa. The chord ends of test specimens were supported by pins, while axial compression was applied via braces. The following design equation was proposed to determine the static ultimate capacity of the investigated DBB T-joints:

$$N_{Ono} = f_{y0} t_0^2 \left[\frac{1}{0.211 - 0.147\left(b_1/b_0\right)} + \frac{b_0/t_0}{1.794 - 0.942\left(b_1/b_0\right)} \right] f\left(n'\right) \qquad (1)$$

In order to assess the suitability of Eq. (1) for CFHSS DBB joints studied in this work, a material factor (C_f) equal to 0.80 was multiplied to Eq. (1). The revised nominal strength was symbolised by $\hat{N}_{Ono}$. The function $f(n')$ is equal to $1 + 0.3n' - 0.3(n')^2$. The chord stress parameter (n') is equal to $0.25N_f(L_0-h'_1)$.

Peña and Chacón (2014)

Peña and Chacón (2014) numerically investigated the static behaviour of DBB X-joints. The numerical investigation was based on elasto-plastic material curves, where the yield strengths of braces and chords were assumed as 235, 275 and 460 MPa. In the numerical investigation, both compression and tensile loads were applied to the FE specimens via braces. Based on the parametric FE results, the following design equation was proposed to determine the static ultimate resistances of the investigated joints:

$$N_{PC} = \left(\frac{1}{1.05}\right) f_{y0} \left[\frac{\left(6.06 - 5.6\beta + 11.4\beta^2\right)\left(0.6 + 1.97\sqrt{\beta}\right) t_0^2}{\left(6.06 - 5.6\beta + 11.4\beta^2\right)\frac{t_0}{b_0} + \frac{\left(0.6 + 1.97\sqrt{\beta}\right)}{3}} \right] \tag{2}$$

The appropriateness of Eq. (2) for CFHSS DBB joints was examined by multiplying the Eq. (2) with C_f=0.80. After multiplying the C_f factor to Eq. (2), the revised nominal strength was symbolised by $\hat{N}_{PC}$.

Chen and Wang (2015)

Chen and Wang (2015) proposed a design equation (Eq. (3)) to predict the ultimate resistances of DBB T-joints with nominal 0.2% proof stress of 235 MPa. The chord ends of test specimens were supported by pins, while axial compression was applied via braces.

$$N_{CW} = 1.814\beta^{\frac{1}{2}}\gamma^{\frac{1}{2}}\tau^{\frac{1}{6}}\left(\frac{1-\beta}{k_n}\right)\left[Q_f\,\frac{f_{y0}t_0^2}{\sin\theta_1}\left(\frac{2\beta}{(1-\beta)\sin\theta_1} + \frac{4}{\sqrt{1-\beta}}\right)/\,\gamma_{M5}\right] \tag{3}$$

In order to prolong the suitability of Eq. (3) for CFHSS DBB joints studied in this work, C_f=0.80 was multiplied to Eq. (3). After multiplying the C_f factor to Eq. (3), the revised nominal strength was symbolised by $\hat{N}_{CW}$. In Eq. (3), f_{y0} is the yield stress of the chord member, γ_{M5} is the partial safety factor of tubular joints as per EC3 (2021) and θ_1 represents angle between brace and chord members (in degrees).

EC3 (2021)

The design equations given in EC3 (2021) are applicable for tubular joints with steel grades up to S700. However, a material factor (C_f) is required to be multiplied with the design rules when the steel grade exceeds S355. When steel grade ranged between 550-700 MPa, the value of material factor (C_f) is equal to 0.80. Furthermore, EC3 (2021) explicitly recommended the value of partial safety factor for tubular joints (γ_{M5}) equal to 1.0. The nominal strengths of joints failed by chord failure mode can be determined as follows:

For CHS-to-CHS T-joint:

$$\hat{N}_{EC3,T} = \frac{C_f}{\gamma_{M5}}\left[Q_f \frac{f_{y0}t_0^2}{\sin\theta_1}\left(2.6+17.7(\beta')^2\right)\gamma^{0.2}\right] \tag{4}$$

For CHS-to-CHS X-joint:

$$\hat{N}_{EC3,X} = \frac{C_f}{\gamma_{M5}}\left[Q_f \frac{f_{y0}t_0^2}{\sin\theta_1}\left(\frac{2.6+2.6\beta'}{1-0.7(\beta')}\right)\gamma^{0.15}\right] \tag{5}$$

Reliability analysis

In order to examine the reliability of existing and proposed design equations, a reliability study was performed as per AISI S100 (2016). The Eq. (6) was used to calculate the reliability index (β_0). In this investigation, a lower bound value of 2.50 was taken as the target β_0. Therefore, when $\beta_0 \geq 2.50$, the design equation was treated as reliable in this study.

$$\beta_0 = \frac{\ln(C_\phi M_m F_m P_m / \phi)}{\sqrt{V_M^2 + V_F^2 + C_P V_P^2 + V_Q^2}} \tag{6}$$

A dead load (DL)-to-live load (LL) ratio of 0.20 was used to compute the calibration coefficient (C_ϕ) in Eq. (6). For the material factor, the mean value and COV are respectively denoted by M_m and V_M. For the fabrication factor, the mean value and COV are respectively denoted by F_m and V_F. Referring to AISI S100 (2016), the M_m and V_M were adopted as 1.10 and 0.10, respectively. Additionally, F_m and V_F were adopted as 1.00 and 0.10, respectively. The resistance factor required to convert the nominal strength to design strength is denoted by ϕ. The mean value of ratios of test and FE strengths-to-nominal strengths predicted from literature and code was denoted by P_m, while the corresponding COV was denoted by V_P. The correction factor (C_P) proposed by AISI S100 (2016) was also used in Eq. (6) to incorporate the effect of the number of data under consideration. Besides, V_Q denoted the COV of load effects. To evaluate the reliability levels of EC3 (2021) design provisions, the DL and LL were combined as 1.35DL + 1.5LL as per EN (2002), and thus, the calculated value of C_ϕ was 1.463. Further, to examine the reliability levels of design equations given in the literature (Chen and Wang, 2015; Ono et al., 1991; Peña and Chacón, 2014) as well as for the proposed design rules, the DL and LL were combined as 1.2DL + 1.6LL as per ASCE 7 (2016), and the calculated value of C_ϕ was 1.521. For extreme cases, where the values of P_m were very small, the calculated values of β_0 were less than zero. Therefore, such values of β_0 are not reported in this paper.

Comparisons between test and FE strengths with nominal strengths

Table 4 presents the summary of overall comparisons of $N_{f,T}$ and $N_{max,T}$ of DBB T-joint test and parametric FE specimens with nominal strengths predicted from Chen and Wang (2015), Ono et al. (1991), Peña and Chacón (2014) and EC3 (2021). The comparisons of the $N_{f,T}$ of DBB T-joints with nominal strengths revealed that the predictions from design rule given in Ono et al. (1991) were very unconservative, quite dispersed and unreliable. The predictions of design rule proposed by Chen and Wang (2015) were slightly unconservative and unreliable for the $N_{f,T}$ of DBB T-joints. However, the predictions from design rule given in Peña and Chacón (2014) were found to be satisfactory but unreliable for the $N_{f,T}$ of DBB T-joints. On the contrary, the comparisons of predictions from CHS-to-CHS T-joint design rule given in EC3 (2021) with the $N_{f,T}$ of DBB T-joints were found to be very conservative but quite dispersed and unreliable. From the comparisons of the $N_{max,T}$ of DBB T-joint test and parametric FE specimens with nominal strengths, it can be noticed that the predictions from the design rule given in Ono et al. (1991) were unconservative, quite dispersed and unreliable. On the other hand, the predictions from design rules given in Chen and Wang (2015) and Peña and Chacón (2014) were quite conservative but dispersed for the $N_{max,T}$ of DBB T-joints. In addition, for the $N_{max,T}$ of DBB T-joints, the CHS-to-CHS T-joint design rule of EC3 (2021) was found to be significantly conservative but quite dispersed. Figs. 11(a) and 11(b) graphically present the comparisons of $N_{f,T}$ and $N_{max,T}$ of DBB T-joint test and parametric FE specimens with nominal strengths predicted from design equations given in Chen and Wang (2015) and Ono et al. (1991), respectively.

The summary of overall comparisons of $N_{f,X}$ and $N_{max,X}$ of DBB X-joint test and parametric FE specimens with nominal strengths predicted from Chen and Wang (2015), Ono et al. (1991), Peña and Chacón (2014) and EC3 (2021) are presented in Table 5. The predictions from design rules given in Chen and Wang (2015), Ono et al. (1991) and Peña and Chacón (2014) were found to be very unconservative, quite dispersed and unreliable for the $N_{f,X}$ of DBB X-joints. On the contrary, the comparisons of predictions of CHS-to-CHS X-joint design rule of EC3 (2021) with the $N_{f,X}$ of DBB X-joints were found to be conservative but dispersed and unreliable. With regard to the comparisons with the $N_{max,X}$ of DBB X-joints, the predictions from design rule given in Ono et al. (1991) were found to be very unconservative, quite dispersed and unreliable. The predictions from design rule given in Chen and Wang (2015) were slightly unconservative and unreliable for the $N_{max,X}$ of DBB X-joints. However, design rule given in Peña and Chacón (2014) satisfactorily predicted the $N_{max,X}$ of DBB X-joints, however, the design equation was found to be unreliable. On the contrary, the comparisons of predictions of CHS-to-CHS X-joint design rule of EC3 (2021) with the $N_{max,X}$ of DBB X-joints were found to be very conservative and uneconomical. Figs. 12(a) and 12(b) graphically present the comparisons of $N_{f,X}$ and $N_{max,X}$ of DBB X-joint test and parametric FE specimens with nominal strengths predicted from design equations given in Peña and Chacón (2014) and Ono et al. (1991), respectively.

Discussion of comparison results

This section of the paper presents the possible reasons behind the inaccuracies of existing design rules for the static strength predictions of CFHSS DBB T- and X-joints. Ono et al. (1991) carried out tests on DBB T-joints made of normal strength steel. A total of twenty-five DBB T-joints was tested, and the obtained test results were used to propose the semi-empirical design rule given by Eq. (1). The simplified theoretical ring model, originally used to formulate the design rule for conventional CHS-to-CHS joints, was employed to develop the Eq. (1). The analytical model was derived using the strain distribution in the chord member as well as assuming that the chord deformation only depends on β. However, strain distribution in the chord of conventional CHS-to-CHS T-joint is quite different to those of DBB T-joint. Furthermore, it has also been reported by Mang (1978) and Kurobane (1981) that the joint strength appreciably decreased as the ratio of yield stress-to-ultimate stress increased, which is one of the characteristics of HSS. In order to calibrate the theoretical ring model for DBB T-joints, numerical parameters in Eq. (1) were derived by curve fitting the test data. Owing to these possible reasons, the design equation given in Ono et al. (1991) yielded very unconservative predictions for the investigated CFHSS DBB joints.

The design rule proposed by Peña and Chacón (2014) for DBB X-joint was derived using the design equation given in Owen et al. (2001) for S275 steel grade DBB X-joints. However, using a reduction factor, Peña and Chacón (2014) numerically extended the validity of the design equation proposed by Owen et al. (2021) up to S460 steel grade. Nonetheless, the revised design equation was found to be inadequate for CFHSS DBB T- and X-joints investigated in this work. More importantly, one of the critical geometric parameters, 2γ (b_0/t_0), affecting the behaviour of DBB joints was left out from the design rule given in Peña and Chacón (2014).

Chen and Wang (2015) proposed design rule for DBB T-joints by applying correction factors to the conventional RHS T-joint design equation given in CIDECT (2009). However, it is worth mentioning that the structural behaviour of DBB T- and X-joints is very different compared to conventional RHS T-joints. Therefore, the extension of the RHS T-joint design rule for DBB T-joint by merely applying correction factors on the former could lead to inaccurate joint strengths. Further, it is essential to note that the design rule given in Chen and Wang (2015) was only valid for Q235 steel grade tubular members. The COV of the proposed design equation (Eq. (3)) was 0.323 (Chen and Wang, 2015), which in turn revealed that the predictions of Eq. (3) were highly dispersed even for the investigated Q235 steel DBB T-joints. Owing to the (1-β) factor in Eq. (3), the strength of the DBB T-joint decreased as the value of β increased, which was contrary to the general behaviour of DBB joints. Moreover, the influence of chord-in-plane bending was considered using functions present in both the numerator and denominator of Eq. (3), which eventually eliminated the total chord-in-plane bending influence from the joint strength. The points mentioned above could be the possible reasons behind the inaccuracies of the design rule given in Chen and Wang (2015) for the investigated CFHSS DBB joints.

In this study, the comparisons of N_f and N_{max} of DBB T- and X-joints with nominal strengths predicted from CHS-to-CHS T- and X-joints design rules given in EC3 (2021) are presented only for illustrative purposes. The design rules for DBB joints are not given in EC3 (2021). The CHS-to-CHS T- and X-joints design rules in previous and latest versions of Eurocode 3 (part-8) are semi-empirical in nature. These design equations (refer to Eqs. (4) and (5)) were developed by calibrating the simplified analytical ring model primarily against the test results of CHS-to-CHS T- and X-joints made of mild steel grades (i.e. steel grades lower than and equal to S355). Although the overall configuration of DBB T- and X-joints looks similar to those of CHS-to-CHS T- and X-joints, however, the interlocking of corner regions of brace and chord members remarkably enhanced the stiffness and strength of DBB T- and X-joints. As a result, current CHS-to-CHS T- and X-joints design rules given in EC3 (2021) provided very conservative predictions for the range of DBB T- and X-joints investigated in this study.

Proposed design rules

In this study, two types of design rules are proposed, under proposal-1 and -2, to predict the N_f and N_{max} of cold-formed S960 steel grade DBB T- and X-joints. Under proposal-1, new design equations are proposed to predict the N_f and N_{max} of DBB T- and X-joints by taking into consideration the effect of important geometric factors as well as P_m and V_p of the overall comparison. However, under proposal-2, the N_f and N_{max} of CFHSS DBB T- and X-joints were predicted by applying correction factor(s) on the current CHS-to-CHS joint design rules (Eqs. (4) and (5)) given in EC3 (2021). Furthermore, as welds were modelled in all parametric FE specimens, the effects of weld and associated WHAR were implicitly included in the proposed design equations. In order to calculate design strengths (N_d), the proposed nominal strengths (N_{pn1} and N_{pn2}) shall be multiplied by their correspondingly recommended resistance factors (ϕ), i.e. $N_d = \phi$ (N_{pn1} or N_{pn2}). All design rules proposed in this study are valid for $0.20 \leq \beta \leq 0.80$, $0.20 \leq \beta' \leq 0.84$, $16.6 \leq 2\gamma \leq 40$, $0.50 \leq \tau \leq 1.28$ and $15° \leq \omega$ (brace) $\leq 63°$. Compared to the existing design rules, the proposed design rules are more accurate, less dispersed and reliable for the investigated CFHSS DBB joints.

DBB T-joints failed by chord crown failure (C) mode

For joint failure strength

<u>Proposal-1:</u>

$$N_{pn1} = \frac{f_{y0} t_0^2 \left(0.5\beta' + 1\right)\left(0.1\tau + 1\right)}{\left[0.16 - 0.001\left(2\gamma\right)\right]} \tag{7}$$

<u>Proposal-2:</u>

$$N_{pn2} = 0.6\left(\beta'\right)^{-0.8}\left[\hat{N}_{EC3,T}\right] \tag{8}$$

The term $\hat{N}_{EC3,T}$ in Eq. (8) can be obtained from Eq. (4). The summary of overall comparison results of proposal-1 and -2 are shown in Table 4. The comparisons of $N_{f,T}$ of test and FE specimens with nominal strengths predicted from Chen and Wang (2015), Ono et al. (1991) and proposal-1 are graphically presented in Fig. 11(a). In addition, the distributions of the ratios of $N_{f,T}$ of test and FE specimens-to-nominal strengths predicted from existing and proposal-1 design rules are shown in Fig. 13.

For joint ultimate capacity

<u>Proposal-1:</u>

$$N_{pn1} = \frac{f_{y0} t_0^2 \left(0.4\beta' + 0.75\right)\left(0.12\tau + 0.94\right)}{\left[0.09 - 0.0007\left(2\gamma\right)\right]} \tag{9}$$

<u>Proposal-2:</u>

$$N_{pn2} = 0.75\left(\beta'\right)^{-0.9}\left[\hat{N}_{EC3,T}\right] \tag{10}$$

The term $\hat{N}_{EC3,T}$ in Eq. (10) can be obtained from Eq. (4). The summary of overall comparison results of proposal-1 and -2 are shown in Table 4. The comparisons of $N_{max,T}$ of test and FE specimens with nominal strengths predicted from Chen and Wang (2015), Ono et al. (1991) and proposal-1 are graphically presented in Fig. 11(b). In addition, the distributions of the ratios of $N_{max,T}$ of test and FE specimens-to-nominal strengths predicted from existing and proposal-1 design rules are shown in Fig. 14.

DBB X-joints failed by chord crown failure (C) mode

For joint failure strength

Proposal-1:

$$N_{pn1} = \frac{f_{y0} t_0^2 \left(1.5\beta' + 0.6\right)\left(0.1\tau + 1\right)}{\left[0.1 + 0.003\left(2\gamma\right)\right]} \tag{11}$$

Proposal-2:

$$N_{pn2} = \left(\beta'\right)^{-0.25}\left[1.5 - 0.02\left(2\gamma\right)\right]\left[\hat{N}_{EC3,X}\right] \tag{12}$$

The term $\hat{N}_{EC3,X}$ in Eq. (12) can be obtained from Eq. (5). The summary of overall comparison results of proposal-1 and -2 are shown in Table 5. The comparisons of $N_{f,X}$ of test and FE specimens with nominal strengths predicted from Peña and Chacón (2014), Ono et al. (1991) and proposal-1 are graphically presented in Fig. 12(a). In addition, the distributions of the ratios of $N_{f,X}$ of test and FE specimens-to-nominal strengths predicted from existing and proposal-1 design rules are shown in Fig. 15.

For joint ultimate capacity

Proposal-1:

$$N_{pn1} = \frac{f_{y0} t_0^2 \left(1.4\beta' + 0.5\right)\left(0.1\tau + 1\right)}{\left[0.12 - 0.0002\left(2\gamma\right)\right]} \tag{13}$$

Proposal-2:

$$N_{pn2} = 0.6\left(\beta'\right)^{-0.35}\left[2.3 - 0.013\left(2\gamma\right)\right]\left[\hat{N}_{EC3,X}\right] \tag{14}$$

The term $\hat{N}_{EC3,X}$ in Eq. (14) can be obtained from Eq. (5). The summary of overall comparison results of proposal-1 and -2 are shown in Table 5. The comparisons of $N_{max,X}$ of test and FE specimens with nominal strengths predicted from Peña and Chacón (2014), Ono et al. (1991) and proposal-1 are graphically presented in Fig. 12(b). In addition, the distributions of the ratios of $N_{max,X}$ of test and FE specimens-to-nominal strengths predicted from existing and proposal-1 design rules are shown in Fig. 16.

Unified design equation

As the formats of the proposed design equations under proposal-1 (Eqs. (7), (9), (11) and (13)) are identical. Therefore, an attempt has been made to propose a unified design equation to predict the N_f and N_{max} of cold-formed S960 steel grade DBB T- and X-joints that failed by the C mode. The proposed unified design equation, shown in Eq. (15), is valid for $0.20 \le \beta' \le 0.84$, $16.6 \le 2\gamma \le 40$, $0.50 \le \tau \le 1.28$. The values of coefficients (A to F) are given in Table 6.

$$N_{pn1} = f_{y0} t_0^2 \frac{(\mathrm{A}\beta' + \mathrm{B})(\mathrm{C}\tau + \mathrm{D})}{[\mathrm{E} + \mathrm{F}(2\gamma)]} \tag{15}$$

Conclusions

The detailed numerical investigation performed in this study on cold-formed S960 steel grade diamond bird-beak (DBB) T- and X-joints led to the following main conclusions:

- The modelling of welds and inclusion of weld heat affected regions substantially increased the accuracies of predictions from the developed DBB T- and X-joint finite element (FE) models.
- The joint failure strengths (N_f) of all DBB T- and X-joints were governed by 3% ultimate deformation limit criterion.
- The chord crown failure (C) mode was identified as the dominant failure mode for all DBB T- and X-joints investigated in this work. This failure mode was characterised by a visible convex deformation at the chord crown locations. In the load vs chord indentation curves, generally, a stagnant phase was noticed near the peak strengths of DBB T- and X-joints, followed by a gradual reduction of load in their post-ultimate regions.
- The design provisions given in the literature (Chen and Wang, 2015; Ono et al., 1991; Peña and Chacón, 2014) and EC3 (2021) are generally found to be unsuitable and uneconomical for the investigated DBB T- and X-joints.
- Accurate, less dispersed, user-friendly and reliable design equations are proposed, by two approaches, to predict the joint failure strengths and ultimate capacities of cold-formed S960 steel grade DBB T- and X-joints that failed by the chord crown failure (C) mode. Moreover, a new unified design equation is also proposed to predict the static joint failure strengths and ultimate capacities of the investigated DBB T- and X-joints.

Acknowledgement

The work described in this paper was fully supported by a grant from the Research Grants Council of the Hong Kong Special Administrative Region, China (PolyU 15218720).

Data Availability Statement

Some or all data, models, or code that support the findings of this study are available from the corresponding author upon reasonable request.

References

Abaqus/Standard (2017). Version 6.17. USA: K. a. S. Hibbit.

AISI S100 (2016). “North American specification for the design of cold-formed steel structural members.” *AISI S100-16*, American Iron and Steel Institute, Washington, DC.

AISC 360 (2016). “Specification for structural steel buildings.” *ANSI/AISC 360-16*, American National Standards Institute and American Institute of Steel Construction, Chicago.

Amraei, M., Ahola, A., Afkhami, S., Bjork, T., Heidarpour, A. and Zhao, X.L. (2019) “Effects of heat input on the mechanical properties of butt-welded high and ultra-high strength steels” Engineering Structures, 198, 109460.

Amraei, M., Afkhami, S., Javaheri, V., Larkiola, J., Skriko, T., Bjork, T. and Zhao, X.L. (2020) Mechanical properties and microstructural evaluation of the heat-affected zone in ultra-high strength steels, Thin-Walled Structures, 157, 107072.

ASCE 7 (2016). “Minimum Design Loads for Buildings and Other Structures.” *ASCE/SEI 7-16*, American Society of Civil Engineers (ASCE), New York.

AWS (2020). “Structural Welding Code – Steel.” *AWS D1.1/D1.1M-20*, American Welding Society (AWS), Miami.

CEN (2002). “Eurocode: Basis of structural design” *EN 1990 (2002)*, European Committee for Standardization, Brussels, Belgium.

CEN (2005). “Design of Steel Structures-Part 1-8: Design of Joints” *EN 1993-1-8*, European Committee for Standardization, Brussels, Belgium.

CEN (2019). “Cold formed welded structural hollow sections of non-alloy and fine grain steels-Part 2: Tolerances, dimensions and sectional properties” *EN 10219-2-2019*, European Committee for Standardization, Brussels, Belgium.

CEN (2021). "Design of Steel Structures-Part 1-8: Design of Joints" prEN 1993-1-8, European Committee for Standardization, CEN, Brussels, Belgium.

Chen, Y. and Wang, J. (2015). "Numerical study and design equations of square and diamond bird-beak SHS T-joints under axial compression." Thin-Walled Struc, 97, 215-24.

Crockett, P. (1994). Finite element analysis of welded tubular connections. PhD Thesis, University of Nottingham, UK.

Davies, G. and Kelly, R.B. (1995). "Bird Beak Joints in Square Hollow Sections – A Finite Element Investigation." In Proceedings of the fourth Pacific Structural Steel Conference, Singapore, 65-72.

Davies, G., Owen, J.S., Kelly, R.B. (1996). "Bird Beak T-Joints in Square Hollow Sections – A Finite Element Investigation." In Proceedings of the sixth International Offshore and Polar Engineering Conference, Los Angeles, U.S.A., Vol. IV, 22-27.

Hu, Y.F., Chung, K.F., Jin, H., Ban, H. and Nethercot, D.A. (2021). “Structural behaviour of T-joints between high strength S690 steel cold-formed circular hollow sections.” Journal of Constructional Steel Research, 182, 106686.

ISO 14346 (2013). “Static design procedure for welded hollow-section joints – Recommendations.” *ISO 14346-2013*, British Standard International Standards, Geneva.

IIW (2012). “Static design procedure for welded hollow section joints – Recommendations.” *IIW Doc. XV-1402-12 and IIW Doc. XV-E-12-433*, International Institute of Welding,

Paris.
Javidan, F., Heidarpour, A., Zhao, X.L., Hutchinson, C.R. and Minkkinen, J. (2016). “Effect of weld on the mechanical properties of high strength and ultra-high strength steel tubes in fabricated hybrid sections.” Engineering Structures, 118, 16–27.
Kelly, R.B. (1998). "The Influence of Member Orientation on Hollow Section Joint Strength." Ph.D. thesis, University of Nottingham, U.K.
Lan, X., Chan, T.M. and Young, B. (2019). "Structural behaviour and design of high strength steel RHS X-joints." Engineering Structures, 200, 109494.
Lan, X., Chan, T.M. and Young, B. (2020). "Experimental study on the behaviour and strength of high strength steel CHS T-and X-joints." Engineering Structures, 206, 110182.
Li, H.-T., and Young, B. (2018). “Experimental investigation of concrete-filled high-strength steel tubular X joints.” ASCE Journal of Structural Engineering, 144(10): 04018178.
Li, H.T. and Young, B. (2019). “Cold-formed high-strength steel tubular structural members under combined bending and bearing.” ASCE Journal of Structural Engineering, 145(8), 04019081.
Li, Q.Y. and Young, B. (2022a). "Experimental and numerical investigation on cold-formed steel built-up section pin-ended columns." Thin-Walled Structures, 170:108444.
Li, Q.Y. and Young, B. (2022b). “Design of cold-formed steel built-up open section members under combined compression and bending.” Thin-Walled Structures, 172, 108890.
Liu, H.X., Fang, H., Zhu, J.Y. and Chan, T.M. (2021). “Numerical investigation on the structural performance of octagonal hollow section columns.” Structures, 34, 3257-3267.
Ma, J.L., Chan, T.M. and Young, B. (2016). "Experimental investigation on stub-column behavior of cold-formed high-strength steel tubular sections" Journal of Structural Engineering, 142(5), 04015174.
Ma, J.L., Chan, T.M. and Young, B. (2017). "Design of cold-formed high strength steel tubular beams" Engineering Structures, 151, 432-443.
Ma, J.L., Chan, T.M. and Young, B. (2019). "Cold-formed high-strength steel rectangular and square hollow sections under combined compression and bending" Journal of Structural Engineering, 145(12), 04019154.
Ma, J.L., Chan, T.M. and Young, B. (2021). "Cold-formed high strength steel tubular beam-columns" Engineering Structures, 230, 111618.
Ono, T., Iwata, M. and Ishida, K. (1991). "An experimental study on joints of new truss system using rectangular hollow sections." In Tubular Structures. 4th International Symposium, 344-353.
Owen, J.S., Davies, G., and Kelly, R.B. (2001). "The influence of member orientation on the resistance of cross joints in square RHS construction." J Constr Steel Res 57(3), 253-278.
Packer, J.A., Wardenier, J., Zhao, X.L., van der GJ, Vegte and Kurobane, Y. (2009). “Design guide for rectangular hollow section (RHS) joints under predominantly static loading.” Comite´ International pour le Developpement et l’Etude de la Construction TuECbulaire (CIDECT), Design Guide No. 3, 2nd edn., LSS Verlag, Dortmund, Germany.
Pandey, M. and Young, B. (2019a). “Tests of cold-formed high strength steel tubular T-joints.” Thin-Walled Struct, 143, 106200.
Pandey, M. and Young, B. (2019b). “Compression capacities of cold-formed high strength steel tubular T-joints.” J Constr Steel Res, 162, 105650.

Pandey, M. and Young, B. (2020). “Structural performance of cold-formed high strength steel tubular X-Joints under brace axial compression.” Engineering Structures, 208, 109768.

Pandey, M. and Young, B. (2021a). “Ultimate Resistances of Member-Rotated Cold-Formed High Strength Steel Tubular T-Joints under Compression Loads.” Engineering Structures, 244, 112601.

Pandey, M. and Young, B. (2021b). “Post-Fire Behaviour of Cold-Formed High Strength Steel Tubular T- and X-Joints.” Journal of Constructional Steel Research, 186, 106859.

Pandey, M. and Young, B. (2021c). “Static resistances of cold-formed high strength steel tubular non-90° X-Joints.” Engineering Structures, 239, 112064.

Pandey, M. and Young, B. (2021d). “Stress Concentration Factors of Cold-Formed High Strength Steel Tubular T-Joints.” Thin-walled Structures, 166, 107996.

Pandey, M. and Young, B. (2021e). “Experimental Investigation on Stress Concentration Factors of Cold-formed High Strength Steel Tubular X-Joints.” Engineering Structures, 243, 112408.

Pandey, M., Chung, K.F. and Young, B. (2021a). “Design of cold-formed high strength steel tubular T-joints under compression loads.” Thin-Walled Structures, 164, 107573.

Pandey, M., Chung, K.F. and Young, B. (2021b). “Numerical investigation and design of fully chord supported tubular T-joints.” Engineering Structures, 239, 112063.

Pandey, M. and Young, B. (2022). “Effect of Member Orientation on the Static Strengths of Cold-Formed High Strength Steel Tubular X-Joints.” Thin-walled Structures, 170, 108501.

Peña, A. and Chacón R. (2014). "Structural analysis of diamond bird-beak joints subjected to compressive and tensile forces." J Constr Steel Res. 98, 158-166.

Stroetmann, R., Kastner, T., Halsig, A. and Mayr, P. (2018). “Mechanical properties and a new design approach for welded joints at high strength steels.” Hong Kong:Engineering Research and Practice for Steel Construction, 79–90.

SSAB. (2017a). Strenx Tube 900 MH. Data Sheet 2042, Sweden.

SSAB. (2017b). Strenx Tube 960 MH. Data Sheet 2043, Sweden.

Wang, F., Zhao, O. and Young, B. (2019). “Flexural behaviour and strengths of press-braked S960 ultra-high strength steel channel section beams.” Engineering Structures, 200, 109735.

Wang, F., Zhao, O. and Young, B. (2020). “Testing and numerical modelling of S960 ultra-high strength steel angle and channel section stub columns.” Engineering Structures, 204, 109902.

Xu, F., Chen, J. and Chan, T.M. (2017). “Numerical analysis and punching shear fracture based design of longitudinal plate to concrete-filled CHS connections.” Construction and Building Materials, 156, 91-106.

Table 1. Summary of test vs FE strength comparisons for DBB T- and X-joints.

Parameters	DBB T-joints		DBB X-joints	
	$\frac{N_{f,T}}{N_{f,FE}}$	$\frac{N_{\max,T}}{N_{\max,FE}}$	$\frac{N_{f,X}}{N_{f,FE}}$	$\frac{N_{\max,X}}{N_{\max,FE}}$
No. of Data (n)	10	10	10	10
Mean (P_m)	0.98	1.01	1.01	1.01
COV (V_p)	0.022	0.007	0.020	0.016

Table 2. Overall ranges of critical parameters used in numerical study.

Parameters	Validity Ranges
β (b_1/b_0)	[0.20 to 0.80]
β' (b_1'/b_0')	[0.20 to 0.84]
2γ (b_0/t_0)	[16.6 to 40]
τ (t_1/t_0)	[0.50 to 1.28]
ω (brace)	[15° to 63°]
ω (chord)	45°

Table 3. Material properties of RHS member and weld used in parametric FE analyses.

Materials	Measured Material Properties							
	E (GPa)	$\sigma_{0.2}$ (MPa)	$\varepsilon_{0.2}$ (%)	σ_u (MPa)	$0.8\sigma_u$ (MPa)	ε_u (%)	ε_f (%)	n
RHS (150×150×6) *	208.5	1059.1	0.71	1145.7	916.6	1.48	9.37#	5.31
Weld Material@	202.7	965.2	0.68	1023.4	818.7	5.41	17.15$	8.13

Note: * Pandey and Young (2019a); @Pandey and Young (2019b); #fracture strain based on 50 mm gauge length; $fracture strain based on 25 mm gauge length.

Table 4. Comparisons between test and FE strengths with existing and proposed nominal strengths for DBB T-joints failed by chord crown failure (C) mode.

Parameters	Comparisons for Joint Failure Strengths						Comparisons for Joint Ultimate Capacities					
	$\frac{N_{f,T}}{\hat{N}_{CW}}$	$\frac{N_{f,T}}{\hat{N}_{Ono}}$	$\frac{N_{f,T}}{\hat{N}_{PC}}$	$\frac{N_{f,T}}{\hat{N}_{EC3,T}}$	$\frac{N_{f,T}}{N_{pn1}}$	$\frac{N_{f,T}}{N_{pn2}}$	$\frac{N_{\max,T}}{\hat{N}_{CW}}$	$\frac{N_{\max,T}}{\hat{N}_{Ono}}$	$\frac{N_{\max,T}}{\hat{N}_{PC}}$	$\frac{N_{\max,T}}{\hat{N}_{EC3,T}}$	$\frac{N_{\max,T}}{N_{pn1}}$	$\frac{N_{\max,T}}{N_{pn2}}$
Mean (P_m)	0.91	0.58	1.00	1.51	1.00	1.01	1.23	0.86	1.37	2.31	1.00	1.01
Maximum	1.24	0.95	1.19	3.07	1.28	1.18	1.63	1.41	1.67	5.35	1.17	1.19
Minimum	0.56	0.32	0.74	0.61	0.80	0.80	0.77	0.40	0.90	0.75	0.74	0.76
COV (V_p)	0.161	0.276	0.095	0.341	0.077	0.078	0.143	0.293	0.119	0.395	0.086	0.090
Resistance factor (ϕ)	1.00	1.00	1.00	1.00	0.85	0.85	1.00	1.00	1.00	1.00	0.85	0.85
Reliability index (β_0)	1.38	-	1.90	2.08	2.55	2.60	2.48	0.95	2.95	2.77	2.53	2.57

Note: “ - ” denotes not applicable as $\beta_0 < 0$.

Table 5. Comparisons between test and FE strengths with existing and proposed nominal strengths for DBB X-joints failed by chord crown failure (C) mode.

Parameters	Comparisons for Joint Failure Strengths						Comparisons for Joint Ultimate Capacities					
	$\frac{N_{f,X}}{\hat{N}_{CW}}$	$\frac{N_{f,X}}{\hat{N}_{Ono}}$	$\frac{N_{f,X}}{\hat{N}_{PC}}$	$\frac{N_{f,X}}{\hat{N}_{EC3,X}}$	$\frac{N_{f,X}}{N_{pn1}}$	$\frac{N_{f,X}}{N_{pn2}}$	$\frac{N_{\max,X}}{\hat{N}_{CW}}$	$\frac{N_{\max,X}}{\hat{N}_{Ono}}$	$\frac{N_{\max,X}}{\hat{N}_{PC}}$	$\frac{N_{\max,X}}{\hat{N}_{EC3,X}}$	$\frac{N_{\max,X}}{N_{pn1}}$	$\frac{N_{\max,X}}{N_{pn2}}$
Mean (P_m)	0.72	0.39	0.78	1.17	1.00	0.98	0.96	0.52	1.05	1.59	1.00	1.01
Maximum	1.31	0.66	1.17	1.96	1.29	1.20	1.47	0.74	1.39	2.25	1.24	1.29
Minimum	0.38	0.18	0.47	0.75	0.81	0.80	0.58	0.32	0.84	1.10	0.83	0.83
COV (V_p)	0.328	0.360	0.233	0.232	0.088	0.069	0.198	0.219	0.104	0.142	0.087	0.078
Resistance factor (ϕ)	1.00	1.00	1.00	1.00	0.85	0.85	1.00	1.00	1.00	1.00	0.85	0.85
Reliability index (β_0)	0.44	-	0.77	1.83	2.53	2.51	1.47	-	2.07	3.24	2.53	2.57

Note: “ - ” denotes not applicable as $\beta_0 < 0$.

Table 6. Values of coefficients for DBB T- and X-joints unified design rule.

Joint Types	Joint Resistance	Coefficients					
		A	B	C	D	E	F
DBB T-joint	Joint failure strength	0.5	1	0.1	1	0.16	-0.001
	Ultimate capacity	0.4	0.75	0.12	0.94	0.09	-0.0007
DBB X-joint	Joint failure strength	1.5	0.6	0.1	1	0.1	0.003
	Ultimate capacity	1.4	0.5	0.1	1	0.12	-0.0002

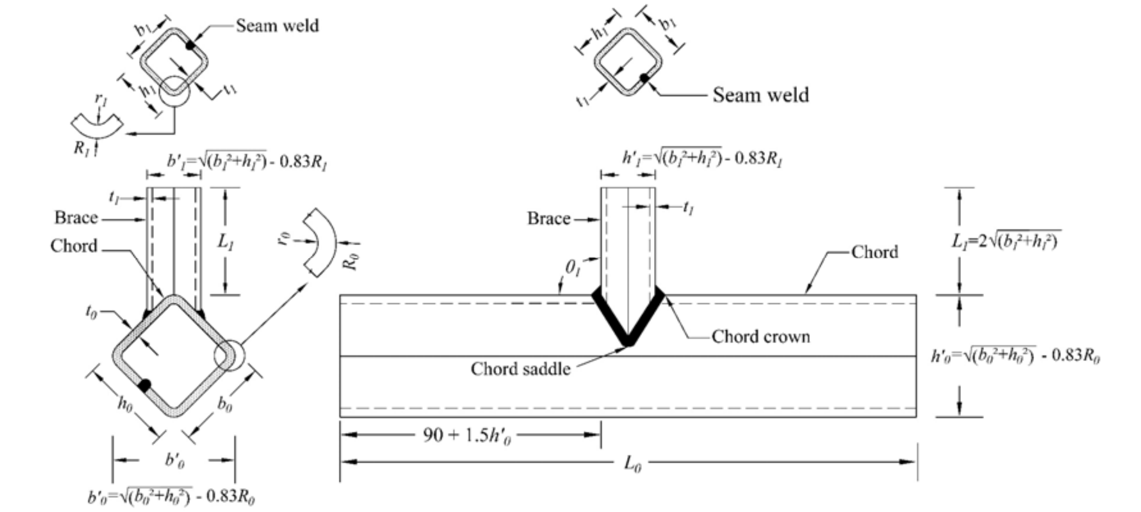

(a) Definitions of notations for DBB T-joint.

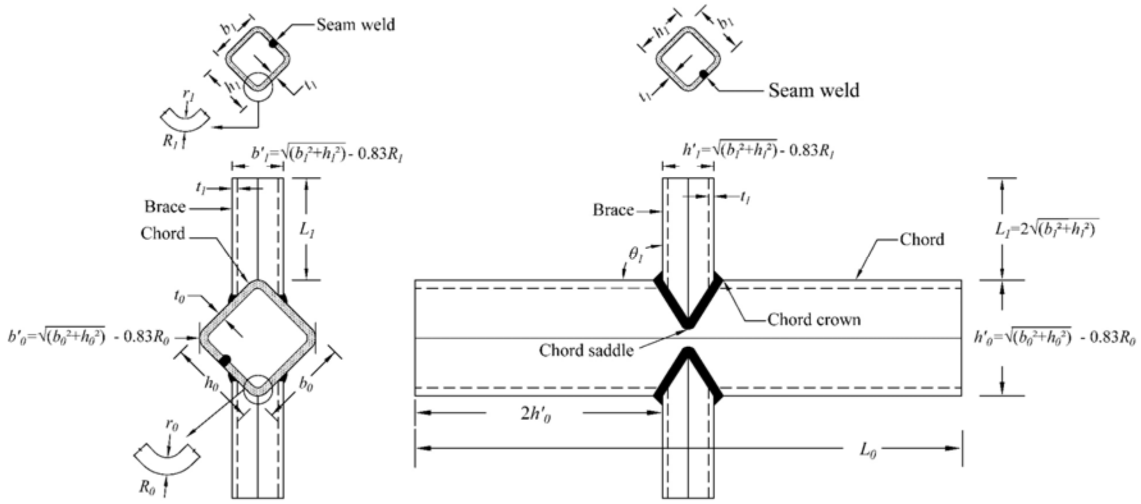

(b) Definitions of notations for DBB X-joint.

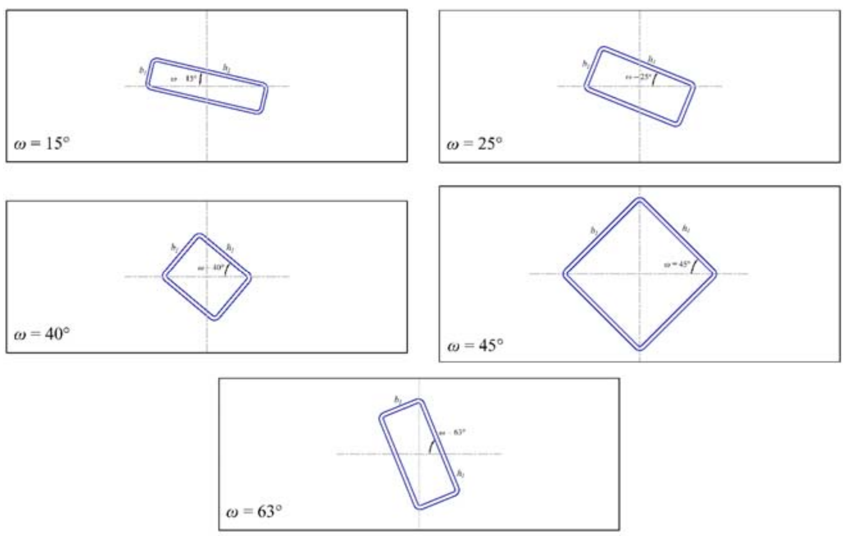

(c) Typical orientations of brace members of DBB T- and X-joints.

Figure 1. Notations definitions and member orientations for DBB T- and X-joints.

Figure 2. Dihedral angle (ψ=120°) for DBB X-joint (also valid for DBB T-joint).

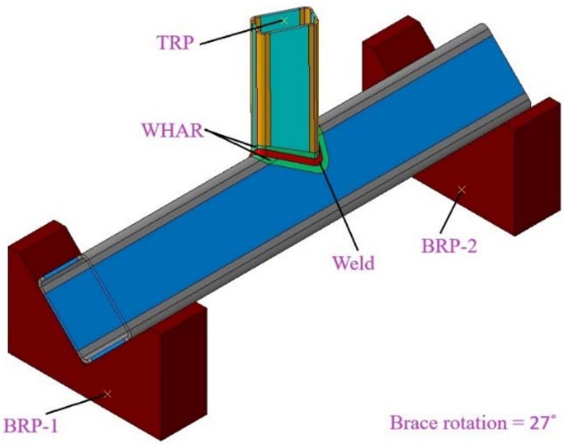

(a) Typical FE model of DBB T-joint with brace rotation of 27°.

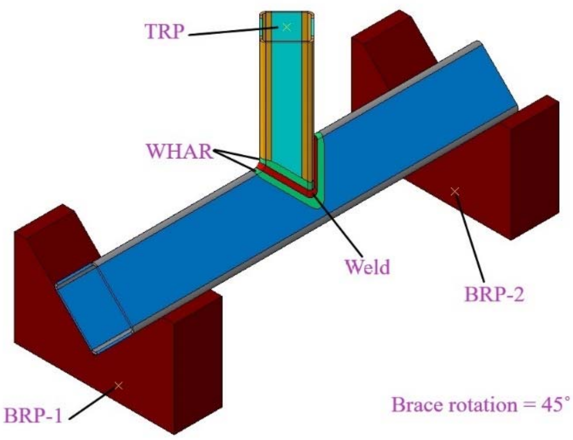

(b) Typical FE model of DBB T-joint with brace rotation of 45°.

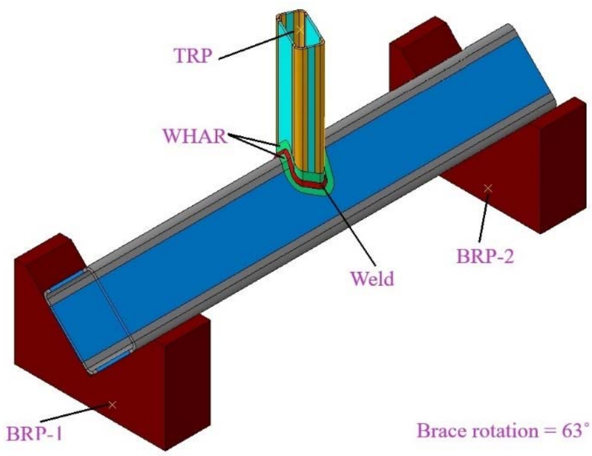

(c) Typical FE model of DBB T-joint with brace rotation of 63°.

Figure 3. Typical FE models of DBB T-joints.

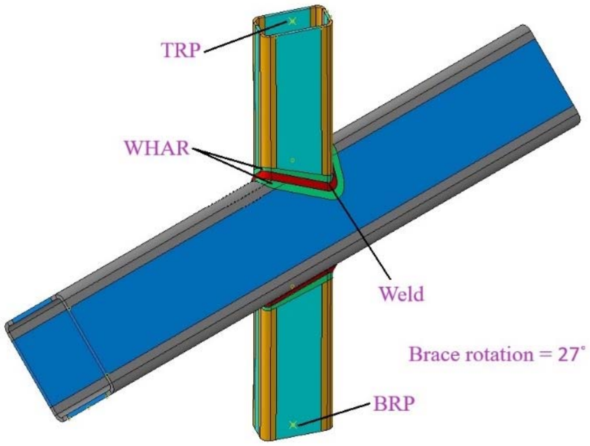

(a) Typical FE model of DBB X-joint with brace rotation of 27°.

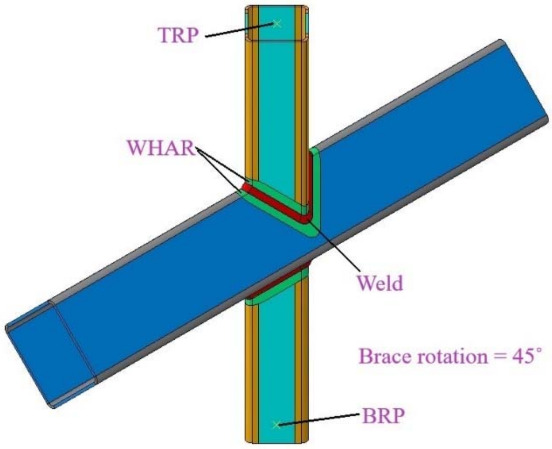

(b) Typical FE model of DBB X-joint with brace rotation of 45°.

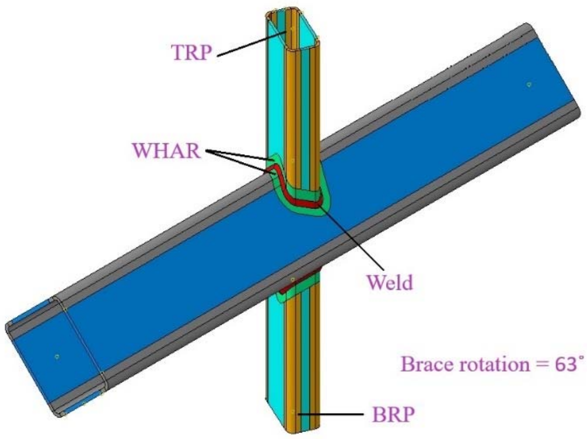

(c) Typical FE model of DBB X-joint with brace rotation of 63°.

Figure 4. Typical FE models of DBB X-joints.

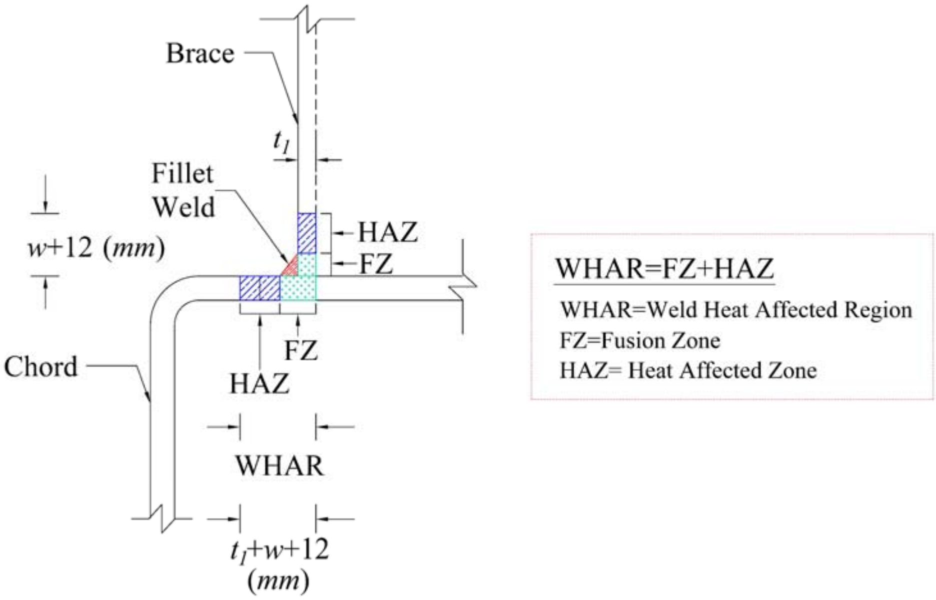

Figure 5. Definition of weld heat affected region (Pandey et al. 2021a).

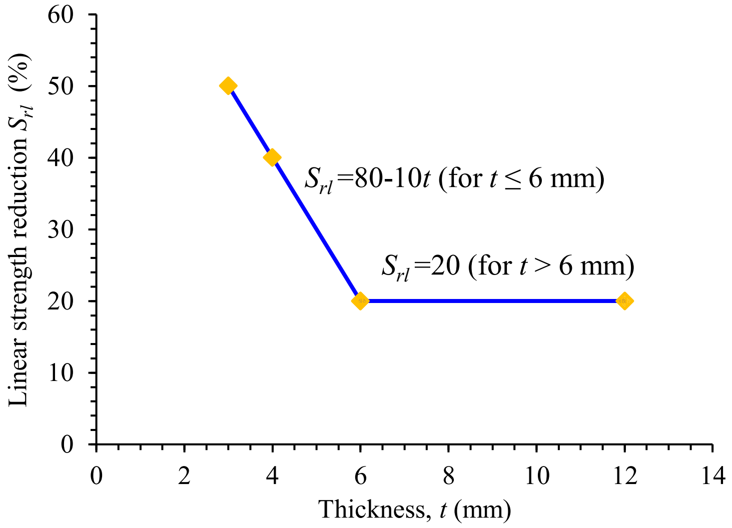

Figure 6. Linear strength reduction model for WHAR of S900 and S960 steel grades tubular joints (Pandey et al. 2021a).

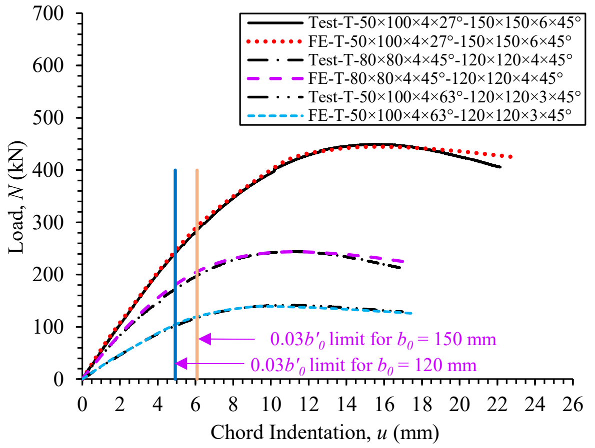

Figure 7. Test vs FE load vs chord indentation (N vs u) curves for DBB T-joints.

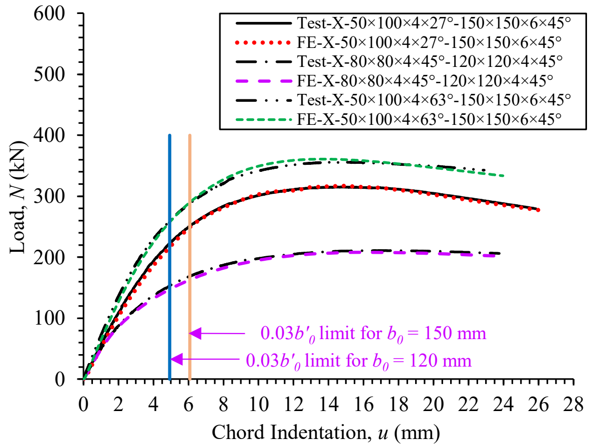

Figure 8. Test vs FE load vs chord indentation (N vs u) curves for DBB X-joints.

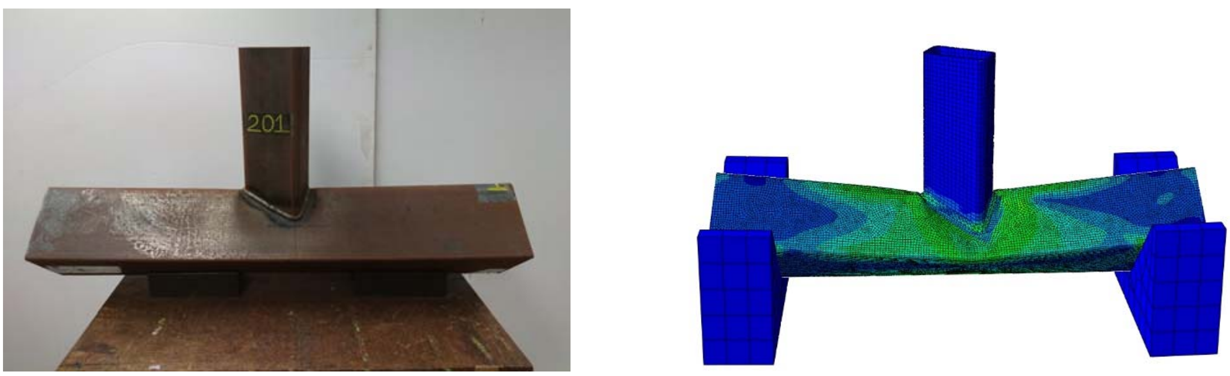

(a) Comparison of test and FE DBB T-joint (ω=27°) failed by chord crown failure (C) mode.

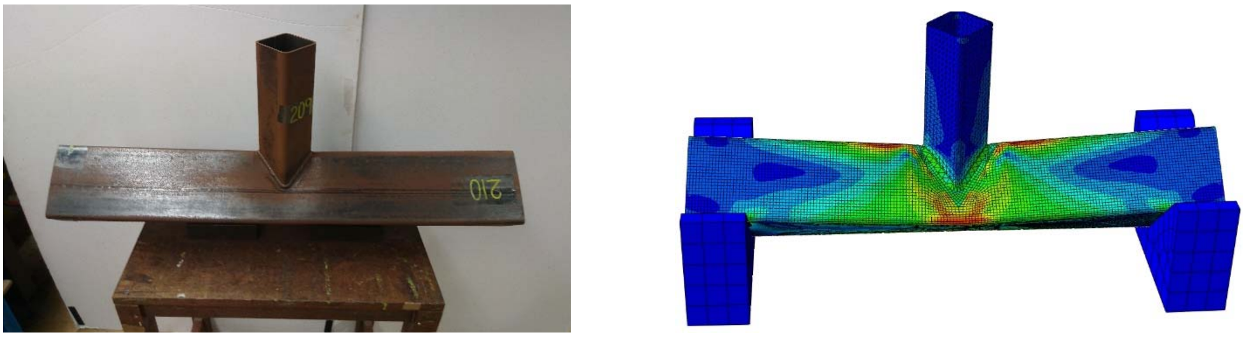

(b) Comparison of test and FE DBB T-joint (ω=45°) failed by chord crown failure (C) mode.

(c) Comparison of test and FE DBB T-joint (ω=63°) failed by chord crown failure (C) mode.
Figure 9. Failure mode comparisons between test and FE specimens of DBB T-joints.

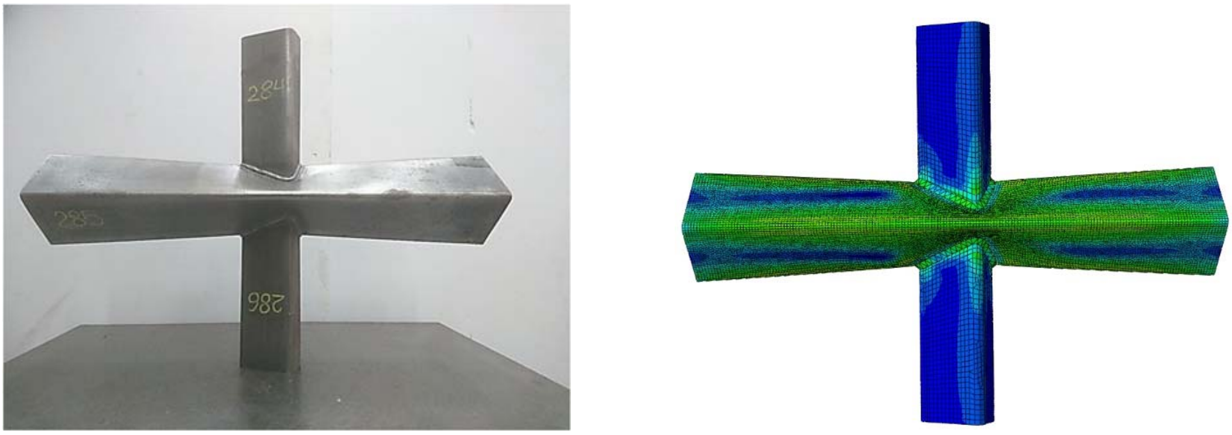

(a) Comparison of test and FE DBB X-joint (ω=27°) failed by chord crown failure (C) mode.

(b) Comparison of test and FE DBB X-joint (ω=45°) failed by chord crown failure (C) mode.

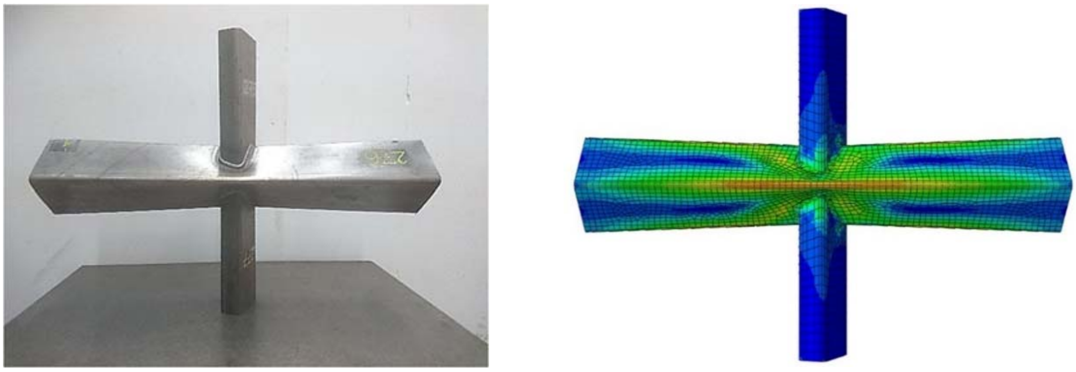

(c) Comparison of test and FE DBB X-joint (ω=63°) failed by chord crown failure (C) mode.
Figure 10. Failure mode comparisons between test and FE specimens of DBB X-joints.

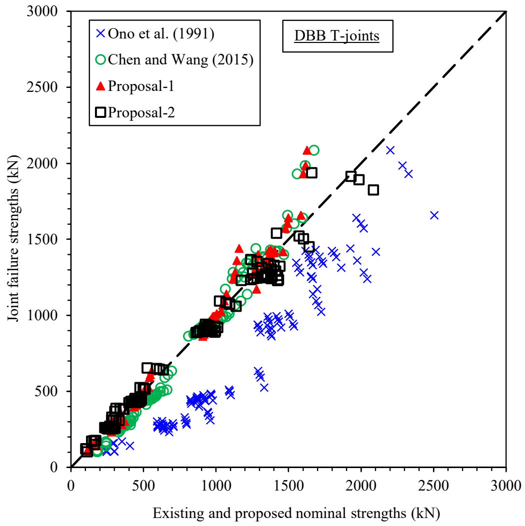

(a) Joint failure strengths ($N_{f,T}$) comparisons for DBB T-joints.

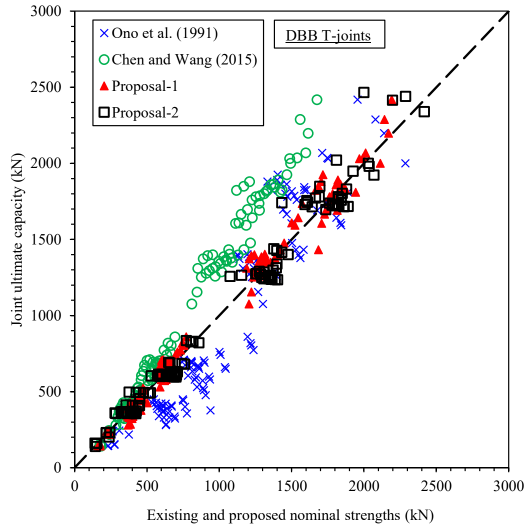

(b) Joint ultimate capacities ($N_{max,T}$) comparisons for DBB T-joints.

Figure. 11. Comparisons of test and FE strengths with current and proposed strengths for DBB T-joints.

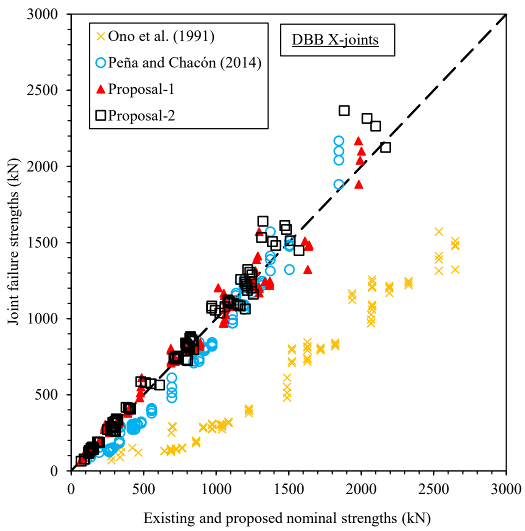

(a) Joint failure strengths ($N_{f,X}$) comparisons for DBB X-joints.

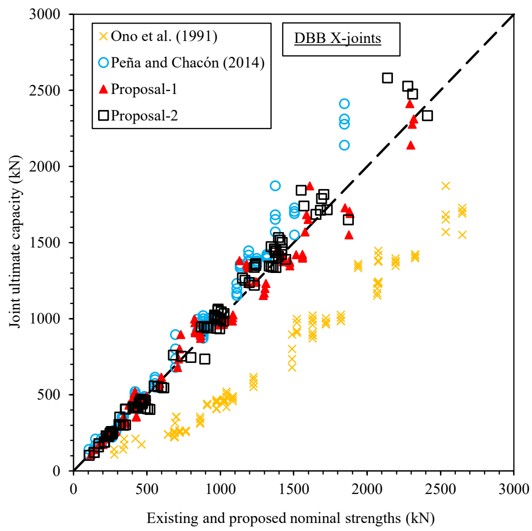

(b) Joint ultimate capacities ($N_{max,X}$) comparisons for DBB X-joints.

Figure 12. Comparisons of test and FE strengths with existing and proposed strengths for DBB X-joints.

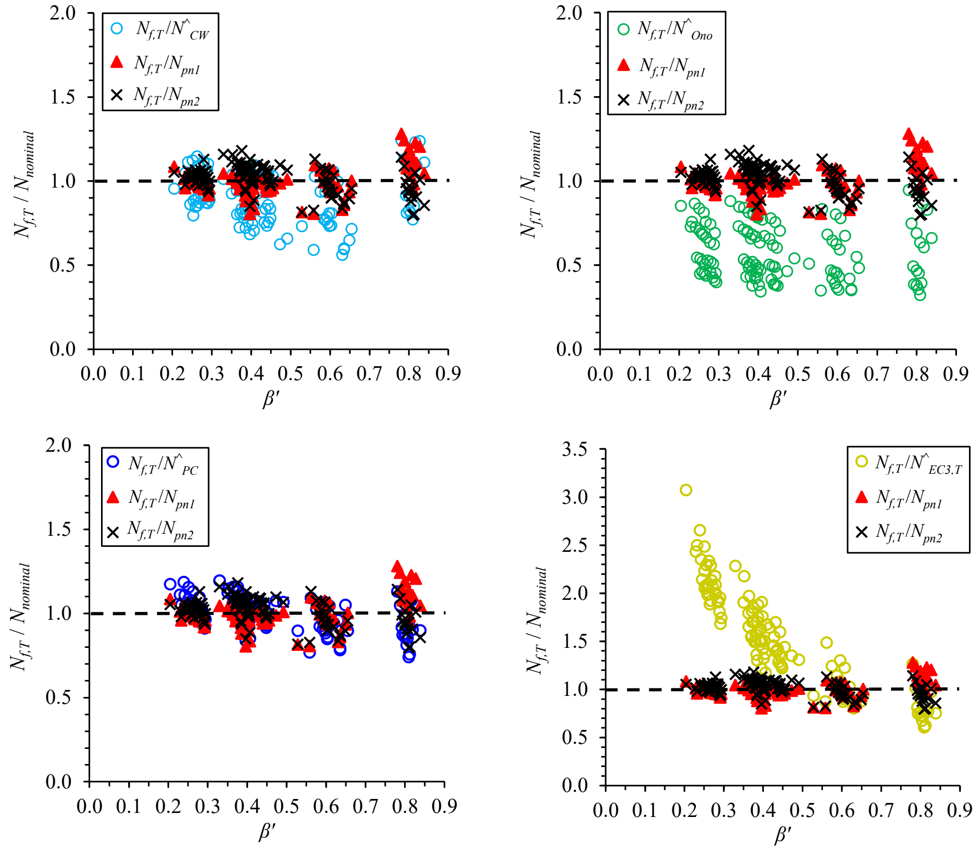

Figure 13. Distributions of joint failure strength comparisons ratios for DBB T-joints.

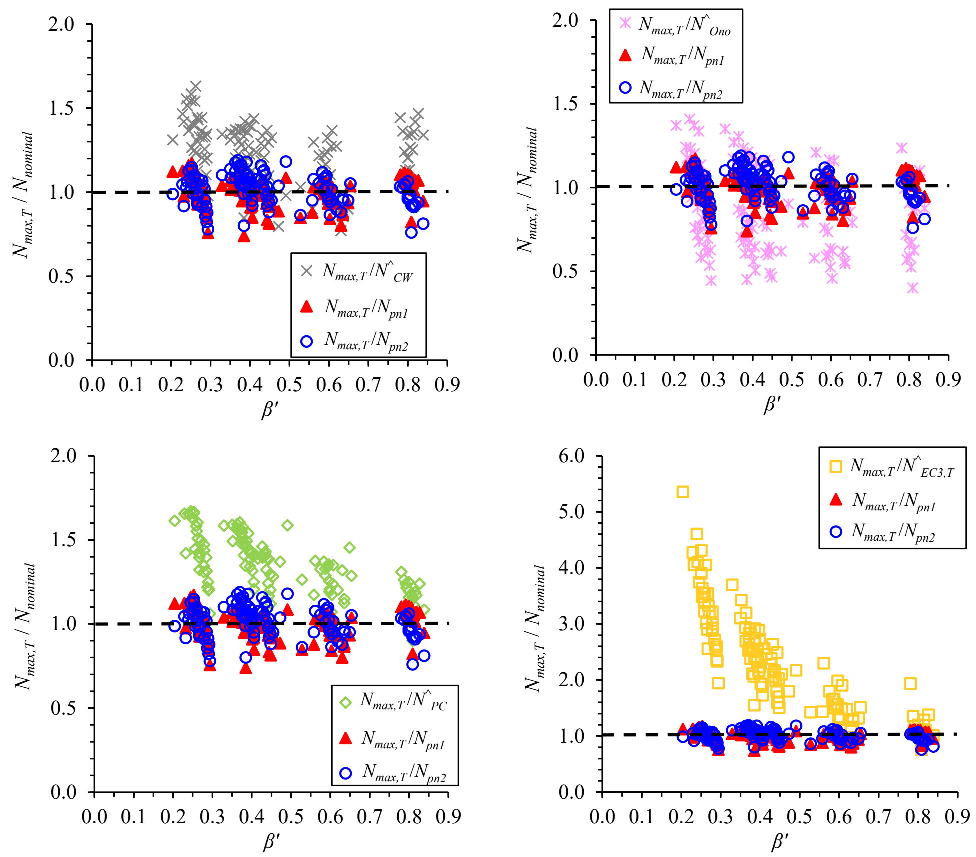

Figure 14. Distributions of joint ultimate capacity comparisons ratios for DBB T-joints.

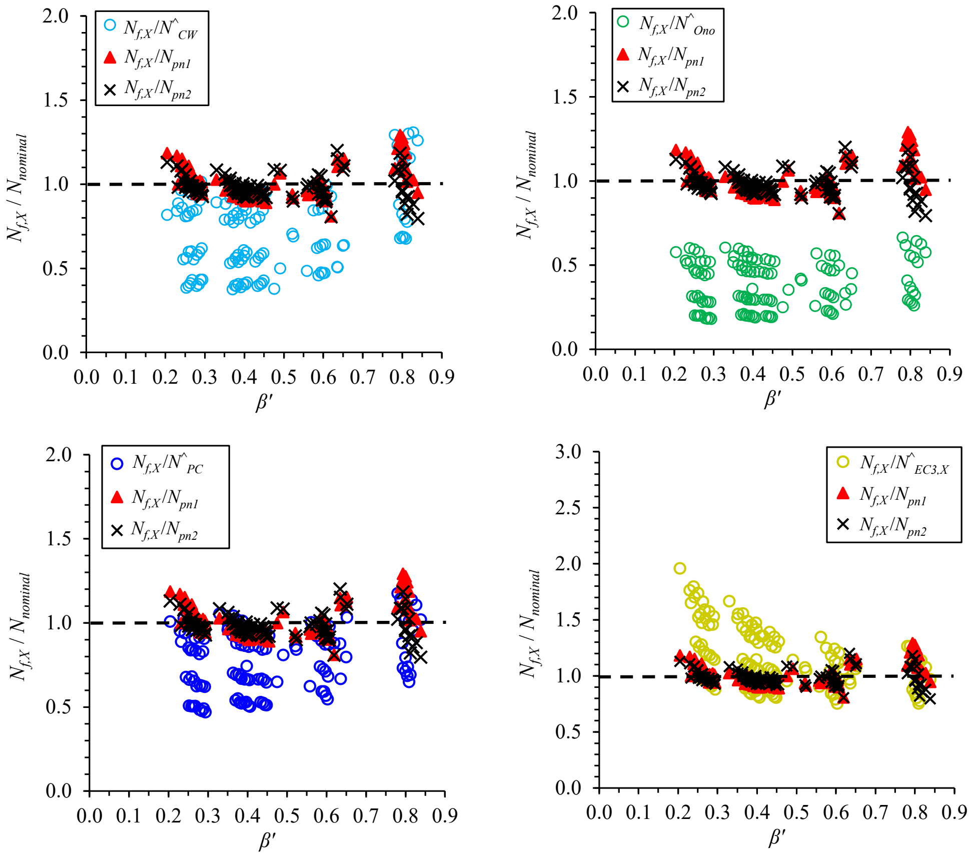

Figure 15. Distributions of joint failure strength comparisons ratios for DBB X-joints.

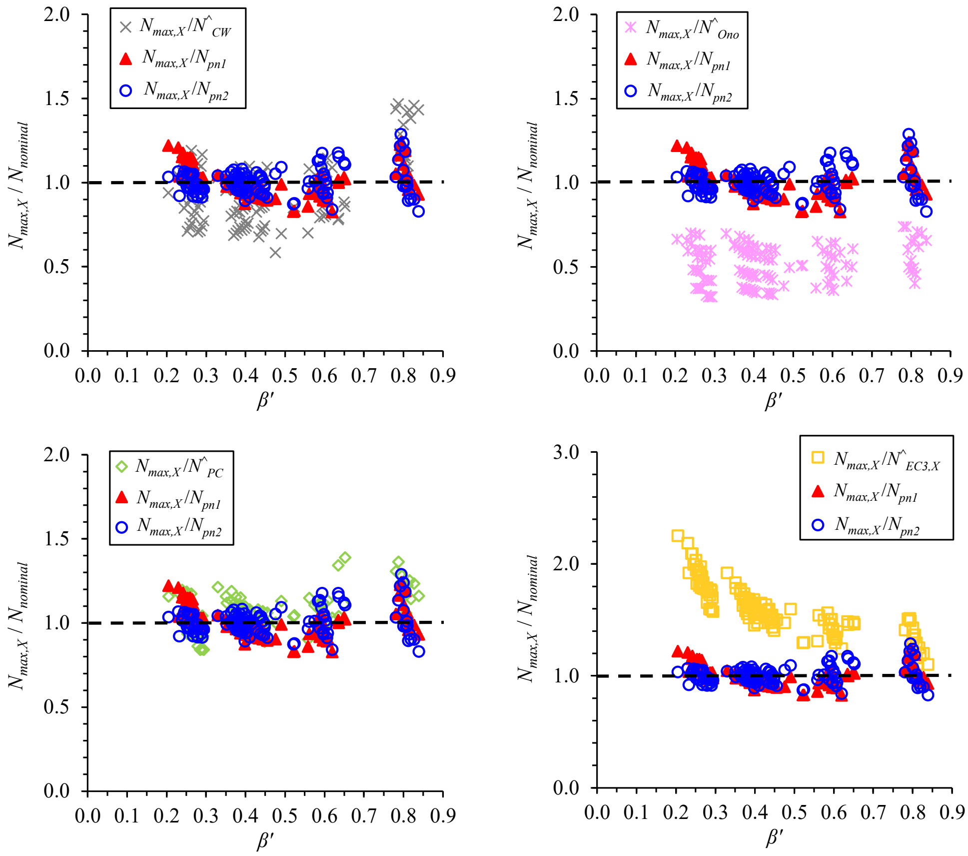

Figure 16. Distributions of joint ultimate capacity comparisons ratios for DBB X-joints.